The proton temperature anisotropy associated with bursty bulk flows in the magnetotail

MingYu Wu,[1,2] Martin Volwerk,[2] QuanMing Lu,[1] Zoltán Vörös,[2] Rumi Nakamura,[2] and TieLong Zhang[1,2]

Received 1 November 2012; revised 1 July 2013; accepted 9 July 2013; published 2 August 2013.

[1] We study the development of the proton temperature anisotropy $T_\perp/T_\parallel$ in bursty bulk flows (BBFs), as observed by THEMIS Mission. For a set of 10 selected events, during which at least three spacecraft are aligned in the same flow, we can sample the plasma parameters along the Earth's magnetotail. The temperature anisotropy in the quiescent tail is negligible. However, as soon as the BBF passes over the spacecraft a strong anisotropy is measured. We analyze $T_\perp/T_\parallel$ as a function of parallel plasma beta-$\beta_\parallel(=nkT_\parallel/(B^2/2\mu_0))$ for the different THEMIS satellites and compare the spread of the data points with various instability thresholds over ion scales that can reduce the temperature anisotropy: for $T_\perp/T_\parallel<1$ the parallel and oblique firehose; for $T_\perp/T_\parallel>1$ the proton cyclotron and mirror mode. It is shown that the anisotropy reduces whilst the BBF is moving Earthward, and the strongest fluctuations are enhanced along the instability thresholds, indicating that these instabilities reduce the proton temperature anisotropy.

Citation: Wu, M. Y., M. Volwerk, Q. M. Lu, Z. Vörös, R. Nakamura, and T. L. Zhang (2013), The proton temperature anisotropy associated with bursty bulk flows in the magnetotail, *J. Geophys. Res. Space Physics*, *118*, 4875–4883, doi:10.1002/jgra.50451.

1. Introduction

[2] In the past decades, there have been many studies of bursty bulk flows (BBFs)-high-speed earthward plasma flows inside the plasma sheet which is the sheet-like region in the center of the magnetotail [*Baumjohann et al*., 1990; *Angelopoulos et al*., 1992]. Satellite observations and theory have suggested that BBFs can be thought as thin filaments with lower entropy as compared to the ambient plasma and have spatial width of 2–3 R_E in the dawn-dusk direction and 1.5–2 R_E in the north-south direction [*Goertz and Baumjohann*, 1991; *Chen and Wolf*, 1999; *Nakamura et al*., 2004]. BBFs are possibly formed during the magnetic reconnection and often associated with substorm onsets [*Baumjohann et al*., 1990, 1991, 1999], and *Angelopoulos et al*. [1994] pointed out that BBFs play a key role in the transport of mass, energy, and magnetic flux in the magnetotail. Besides, BBFs are also the drivers of MHD waves and turbulence [*Bauer et al*., 1995; *Volwerk et al*., 2004; *Vörös et al*., 2004], which will be the main topic of this current paper.

[3] The proton temperature is found to be weakly anisotropic during some BBFs [*Kim et al*., 2010; *Runov et al*., 2010]. These anisotropies can be driven by magnetic reconnection or turbulence [*Drake et al*., 2009; *Liu et al*., 2006]. Proton temperature anisotropy instabilities have been studied in previous works. If the proton velocity distribution in a collisionless proton plasma is approximately bi-Maxwellian and the temperature anisotropy is expressed through $T_\perp$ and $T_\parallel$ (where $T_\perp$ and $T_\parallel$ are the perpendicular and parallel proton temperatures with respect to the ambient magnetic field $\mathbf{B_0}$, respectively), this proton temperature anisotropy can be a source of energy for various instabilities. In the case that the proton temperature $T_\perp>T_\parallel$, the relevant instabilities are mirror and proton cyclotron modes [*Hasegawa*, 1969; *Gary et al*., 1993, 1994]; whilst in the case that the proton temperature $T_\parallel > T_\perp$, the relevant instabilities are parallel and oblique firehose modes [*Quest and Shapiro*, 1996; *Hellinger and Matsumoto*, 2000]. Previous observation and simulation results showed that these instabilities appear to be active in the solar wind [*Kasper et al*., 2002; *Hellinger et al*., 2006], the Earth's bow shock[*Lu and Wang*, 2005; *Lu et al*., 2006], the terrestrial magnetosheath [*Anderson et al*., 1994], and magnetotail [*Vörös*, 2011].

[4] According to marginal stability analysis, the thresholds for the four instabilities mentioned above can be calculated by the following equation:

$$\frac{T_\perp}{T_\parallel} = 1 + \frac{a}{\left(\beta_\parallel - \beta_0\right)^b} \tag{1}$$

where the a, b, and β_0 are the fitted parameters calculated by *Hellinger et al*. [2006] under the assumption that the growth rate $\gamma = 10^{-3}\omega_{cp}$ (where ω_{cp} is the proton cyclotron frequency) for all four wave modes. With the 10 years' measurements by the Wind spacecraft, the relation between the statistical observation results in the solar wind and the linear

[1]School of Earth and Space Sciences, University of Science and Technology of China, Hefei, China.
[2]Space Research Institute, Austrian Academy of Sciences, Graz, Austria.

Corresponding author: Q. Lu, School of Earth and Space Sciences, University of Science and Technology of China, Hefei, 230026 China. (qmlu@ustc.edu.cn)

2169-9380/13/10.1002/jgra.50451

Table 1. The Selected Events for This Paper[a]

Event	Date	Time Interval	SCs	$(x, y, z)(R_E)$
1	2008-02-26	0404 – 0409	B/D/E	(−21.9,4.3,−2.7)/(−10.6,4.2,−1.9)/(−9.8,4.9,−1.6)
2	2008-03-09 (a)	0213 – 0217	B/D/E	(−20.9,7.8,−0.0)/(−9.3,6.4,−0.3)/(−8.0,6.7,−0.1)
3	2008-03-09 (b)	0241 – 0251	B/C/D	(−20.6,7.6,−0.2)/(−16.2,7.5,−0.9)/(−9.6,6.2,−0.5)
4	2008-03-13	0720 – 0735	B/C/E	(−16.6,5.1,−0.8)/(−14.0,5.1,−1.7)/(−10.5,5.1,−1.7)
5	2008-03-17	0846 – 0904	B/C/D/E	(−14.3,4.6,−0.3)/(−12.4,4.1,−1.4)/(−10.2,3.4,−1.4)/(−10.4,4.5,−1.6)
6	2008-03-21	0927 – 0930	B/C/E	(−12.8,4.2,0.1)/(−11.1,3.6,−1.0)/(−10.1,4.5,−1.5)
7	2009-02-23	0834 – 0850	B/C/D/E	(−23.0,−0.7,−1.9)/(−17.0,−2.4,−2.4)/(−10.7,−3.8,−2.2)/(−10.9,−2.9,−2.4)
8	2009-02-27	0750 – 0800	B/C/D/E	(−20.1,−0.6,−1.5)/(−16.7,−1.6,−2.2)/(−11.1,−2.7,−2.2)/(−11.1,−1.7,−2.4)
9	2009-03-03 (a)	0615 – 0630	B/C/E/A	(−16.4,−0.9,−1.1)/(−16.4,−0.8,−1.9)/(−11.1,−0.5,−2.2)/(−11.0,−0.6,−3.1)
10	2009-03-03 (b)	0656 – 0702	C/D/E/A	(−16.8,−0.4,−1.9)/(−11.2,−1.0,−2.1)/(−10.9,0.0,−2.2)/(−10.8,−0.1,−3.1)

[a]Given are the event number, the date, the time interval of the BBF, the spacecraft which observed the BBF, and the x, y, and z components of the spacecraft location in GSM coordinate.

theoretical prediction are analyzed. *Kasper et al.* [2002] pointed out that the observations of proton temperature anisotropy $T_\perp/T_\parallel$ and proton parallel beta $\beta_\parallel$ are found to be constrained by the theoretical threshold of the firehose instability when $T_\perp/T_\parallel<1$. With the same data set, *Hellinger et al.* [2006] presented the comparison between the observations of solar wind and linear predictions for the four instabilities and found that the observed proton temperature anisotropies are well constrained by the mirror mode for $T_\perp>T_\parallel$ and by the oblique firehose mode for $T_\parallel > T_\perp$ in the slow solar wind. Recently, *Bale et al.* [2009] extended the work by *Hellinger et al.* [2006] and found that the magnetic field fluctuations are enhanced along the thresholds of the mirror, proton oblique firehose, and proton cyclotron modes.

[5] In the Earth's magnetotail, ion-scale temperature anisotropy associated relaxation processes, driven by reconnection jets can influence the transport of mass, energy, and magnetic flux during substorms. However, the spatial distribution of the relevant ion-scale instabilities along the magnetotail associated with Earthward propagating BBFs is still not known. In this paper, multipoint observations of BBFs by the five THEMIS probes are used to study the evolution of the proton temperature anisotropy associated with the BBFs along the Earth's magnetotail.

2. Data Set and Selection Criteria

[6] With the THEMIS Mission, it is possible to obtain time series of the various quantities at different locations along the magnetotail, which is helpful to distinguish between the temporal and spatial behavior of the plasma flows in the plasma sheet. There are five spacecraft to the THEMIS Mission which are aligned along the magnetotail. They can observe the fast plasma flows in the same flow channel, which can be used to investigate the evolution of BBFs.

[7] For the event selection, we used the 4 Hz magnetic field data obtained by the Flux Gate Magnetometer [*Auster et al.*, 2008], 3 s spin-average plasma data with energies less than 30 keV from the Electrostatic Analyzers (ESA) [*McFadden et al.*, 2008] and from the Solid State Telescopes (SST) [*Angelopoulos*, 2008] for particles with energies more than 30 keV. The combined ESA and SST measurements are used to improve the quality of the proton data. To survey the BBF events in the plasma sheet, we used the data set from THEMIS between January and April of the years 2008 and 2009, while THEMIS had its apogee in the magnetotail.

[8] For our present study, the BBF events should be observed by multiple (at least three) spacecraft in different locations of the magnetotail. In the Geocentric Solar Magnetospheric coordinate system (GSM), the width of the BBF is about 3 R_E (R_E is the radius of the Earth) in the y direction and 2 R_E in the z direction [*Nakamura et al.*, 2004]. So, the interspacecraft distance should be less than these values in the y and z direction in the selected events. We assume spatially homogeneous steady bi-Maxwellian distributions over the selected $y-z$ interspacecraft distances. In the x direction, the observed time interval of two spacecraft is required to be approximately the plasma propagating time. During the time intervals of the BBF events, the plasma beta β should be greater than 0.5 [*Baumjohann et al.*, 1990] to ensure the spacecraft are in the plasma sheet and the perpendicular component of the BBF's velocity $v_\perp$ should exceed 150 km/s at least once while $v_\perp$ maintains a minimum level of 100 km/s. Each BBF is defined to begin when its velocity exceeds 100 km/s and ends when the velocity drops below 100 km/s [*Angelopoulos et al.*, 1994]. In addition,

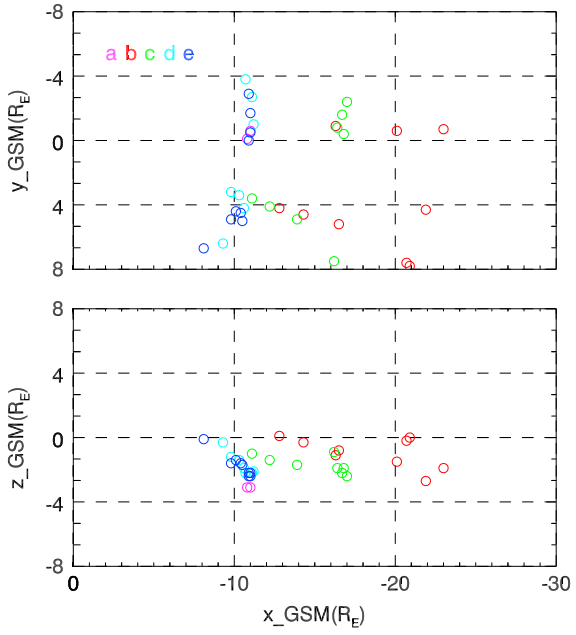

Figure 1. THEMIS spacecraft position in the XY and XZ planes for the 10 events.

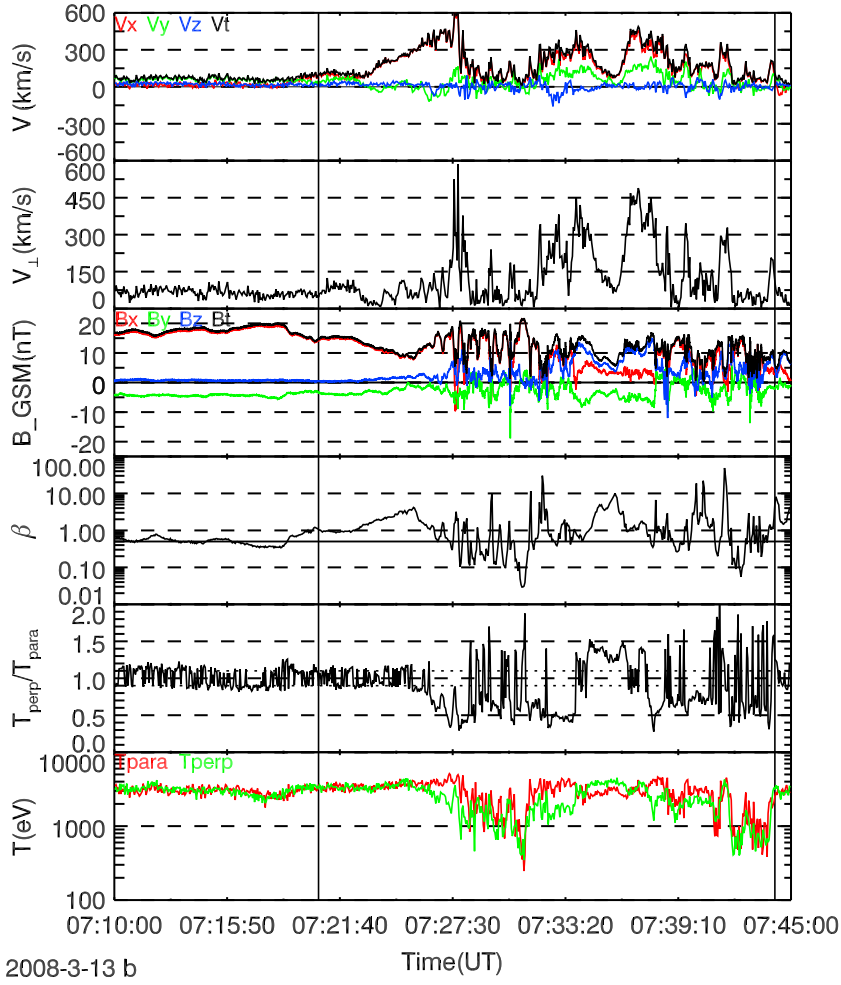

Figure 2. Data from THB on 13 March 2008: from the top panel to the bottom one, they are the velocity of plasma flows (red, cyan, and blue lines are the x, y, and z components of velocity, respectively; while the black line represents the total velocity of plasma flows), the perpendicular component of the velocity, the magnetic field (red, cyan, and blue lines are the x, y, and z components of magnetic field, respectively; while the black line represents the magnitude of the magnetic field), the plasma beta, the ratio of $T_\perp/T_\parallel$, and the two components of proton temperature. The time interval of BBF event is between two black vertical bars.

samples of $v_\perp > 150$ km/s that are less than 10 min apart are considered to belong to the same BBF, even if the velocity drops below 100 km/s between these samples.

[9] With these requirements, we have found 10 events, for which the BBFs are observed by at least three spacecraft in the same earthwards dominated flow channel in each event. All these events are listed in Table 1. Figure 1 shows the positions of the THEMIS spacecraft when they observed the BBFs for these 10 events in the GSM XY and XZ planes.

3. Observations

3.1. The Evolution of the Proton Temperature Anisotropy

[10] We first make a case study to analyze the evolution of BBF observed by multiple spacecraft at different locations along the plasma sheet. We present an example BBF event in Figure 2, which shows the plasma and magnetic field data obtained by the THB spacecraft on 13 March 2008. In Figure 2, the top panel shows the three components (x, y, and z) and the total velocity (V_t) of the plasma flows; the second panel shows the perpendicular component of velocity; the third panel gives the x, y, and z component and the total magnetic field; the fourth panel is the plasma beta; the fifth panel shows the ratio of the proton temperature $T_\perp/T_\parallel$; and the bottom panel gives the parallel and perpendicular components of proton temperature. The time interval of the BBF event is between two black vertical bars, while the time interval before the BBF event represents the quiet plasma sheet. Figures 3 and 4 show the plasma and magnetic field data obtained by the THC and THE on the same day, respectively. At the interval of BBF events, the locations of THB, THC, and THE are at (−16.6, 5.1, −0.8), (−14.0, 5.1, −1.7), and (−10.5, 5.1, −1.7) R_E in GSM coordinate, respectively. The maximum of Δy is 0.0 R_E and Δz is 0.9 R_E. Because the BBF can extend about 3 R_E in y direction and 2 R_E in z direction, we can assume that the three satellites observe the same BBF event.

[11] For each 3 s, we calculate the proton temperature anisotropy ratio $T_\perp/T_\parallel$ and the parallel plasma beta $\beta_\parallel$, which

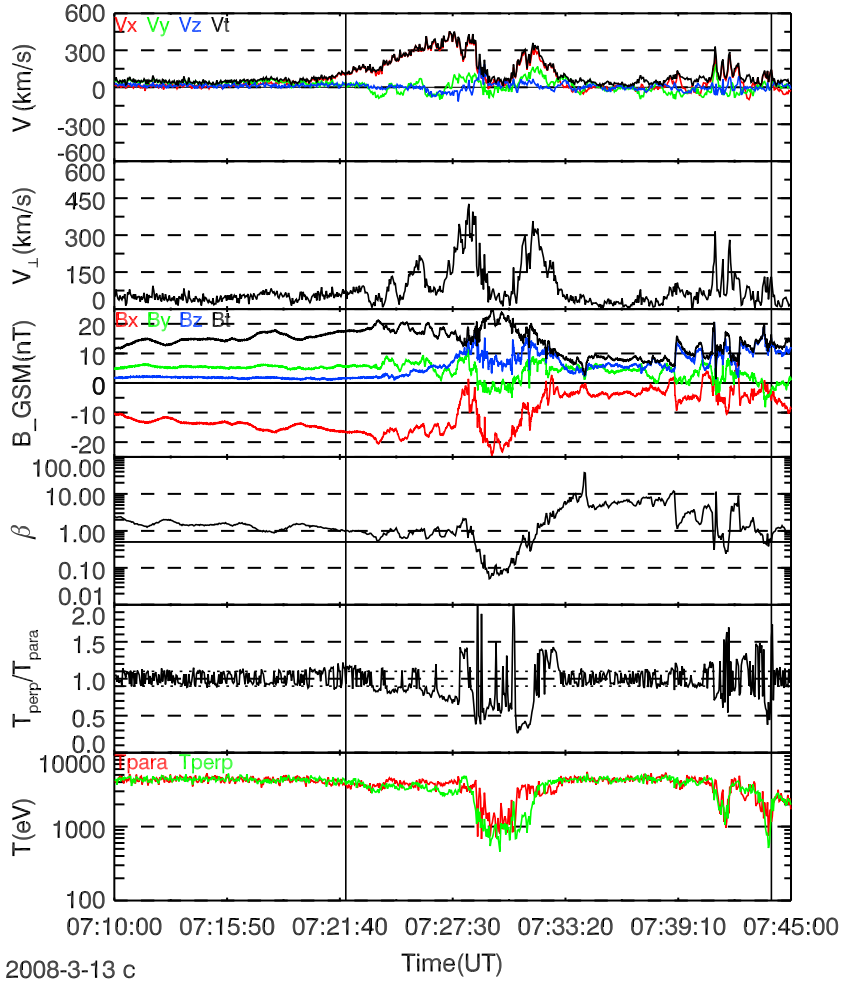

Figure 3. The plasma and magnetic field data from THC on 13 March 2008. The time interval of BBF event is between two black vertical bars.

give us one point in the space ($\beta_{||}$, $T_{\perp}/T_{||}$). During the time interval of the BBF shown in Figures 2–4, the proton temperature anisotropy distribution associated with the BBF in ($\beta_{||}$, $T_{\perp}/T_{||}$) is are shown in Figure 5. From the top to the bottom panel, the results are from the observation by THB, THC, and THE. The overplotted dashed curves are the thresholds of the different instabilities which are calculated from equation (1) with the parameters in Table 1 by *Hellinger et al.* [2006]. In Figure 5, the upper red dashed curve is the threshold of the mirror mode; the black dashed curve is the threshold of the proton cyclotron instability; the bottom black dashed curve is the threshold of the parallel firehose mode; and the bottom red dashed curve is the threshold of the oblique firehose mode. The horizontal green dashed lines show the variation in the temperature ratio calculated during the intervals of quiet time plasma sheet before the BBF (e.g., see the dotted line of the fifth panel in Figure 1), which also gives an estimate of the error in the measurements, assuming the quiet time current should have near-isotropic temperatures. Almost all the data points that remain inside the area, bordered by the theoretical curves of temperature instability thresholds, correspond to stable plasma states. In Figure 5, at high $\beta_{||}$($\beta_{||}$>2), we can observe obvious anisotropy with THB. However, the majority of observations by THC and THE are in the region $0.9<T_{\perp}/T_{||}<1.1$, which are almost isotropic. Comparing the distribution observed by these three satellites, it is found that the anisotropic distribution seems to turn into an isotropic distribution as the BBF propagates to the Earth from -16.6 to -10.5 R_E down the tail.

[12] In all the 10 events, the THB and THC are farther away from the Earth than the other three spacecraft. Therefore, the statistical results of the proton temperature anisotropy distribution observed by THB and THC can show the anisotropy associated with BBF which are far and intermediately away from the Earth, while the statistical results of the other spacecraft can give the information when the BBF is close to the Earth. In Figure 6, the top panel which includes 2851 data points shows the statistic results of THB and THC with all 10 events, and the bottom panel which includes 2484 data points shows the results of the other three spacecraft. The size of every bin is (0.1, 0.1) in ($\beta_{||}$, $T_{\perp}/T_{||}$) space. The dashed curves have the same meaning as in Figure 5. The distribution in the upper panel shows higher anisotropy than the one in the bottom panel. It means that the BBFs have a high anisotropy in the

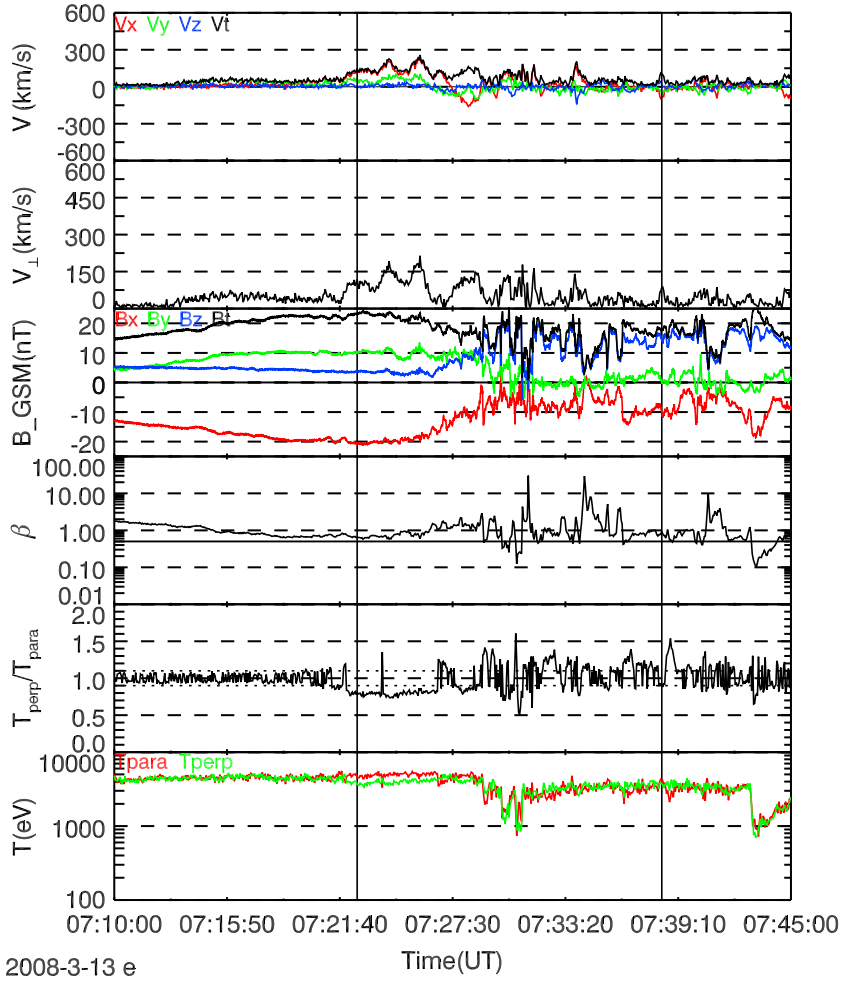

Figure 4. The plasma and magnetic field data from THE on 13 March 2008. The time interval of BBF event is between two black vertical bars.

midmagnetotail and will relax towards isotropy during earthward propagation.

3.2. The Instabilities Generated by the Temperature Anisotropy

[13] The proton temperature anisotropy can drive various instabilities. In Figure 7, we present two color scale plots of the number of events in ($\beta_{\|}$, $T_{\perp}/T_{\|}$) space which are associated with BBF (top panel) and quiet plasma sheet conditions (bottom panel). The top panel which includes 5335 data points shows that the majority of observations lie within the region bounded by the instability threshold (the dashed curves, see above). For $T_{\perp}/T_{\|}>1$, the apparent constraint is compatible with the threshold condition for the mirror instability (the top red dashed curve). The linear predictions for proton cyclotron instability (the top black dashed curve) don't seem to constrain the observations. For $T_{\perp}/T_{\|}<1$, the constraint seems to be more compatible with the oblique firehose (the bottom red dashed curve) than with the parallel (the bottom red dashed curve) for $\beta_{\|}>1$. This distribution shows that the temperature anisotropy associated with the BBFs most likely drives the mirror mode and oblique firehose instabilities, thereby limiting the extent of the $T_{\perp}/T_{\|}$ values. We will come back to this further below.

[14] The bottom panel which includes 6674 data points shows the statistical results of the number of events in ($\beta_{\|}$, $T_{\perp}/T_{\|}$) bins, which are associated with the quiet plasma sheet before the BBF. As shown in Figure 2, the time interval of quiet plasma sheet in each event is a high beta ($\beta > 0.5$) interval prior to the BBF and has no obviously flow. We choose a 10 min interval for each event. In the bottom panel of Figure 7, most of the points are in the region $0.9<T_{\perp}/T_{\|}<1.1$ for $\beta_{\|}>1$. This means that the proton distributions are overall isotropic in the quiet plasma sheet.

[15] Additionally, we investigate the effect of the location of spacecraft on the temperature anisotropy distribution. The top panel of Figure 8 which includes 3022 data points shows the results in the near Earth tail ($|X\_GSM| < 14R_E$), and the bottom panel including 2313 data points shows the results in the regions further down the tail ($|X\_GSM| \geq 14R_E$). Comparing the two figures, we can find that the criteria for the mirror mode could be satisfied in both panels; however, the criteria for the firehose/oblique firehose instability are hardly fulfilled in the near-earth magnetotail ($|X\_GSM| < 14R_E$). Additionally, there are less data points outside of the area bordered by theoretical thresholds in the near-Earth plasma sheet. This

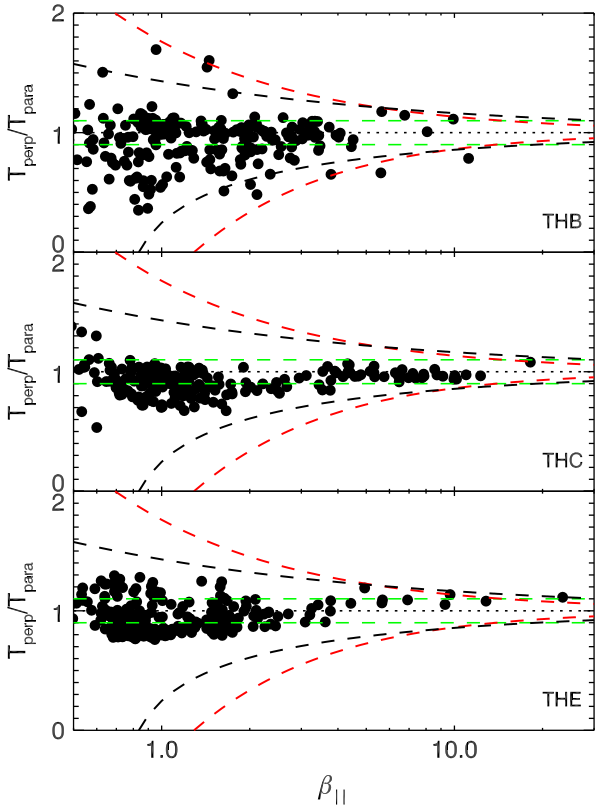

Figure 5. The top panel shows the proton temperature anisotropy distribution associated with the BBF in the space ($\beta_{||}$, $T_{\perp}/T_{||}$) observed by THB. The middle panel shows the results of THC, and the bottom panel shows the one of THE. The four dash curves are the thresholds of four instabilities. The two red dash curves are mirror mode (upper) and oblique firehose mode (bottom), and the two black dash curves are proton cyclotron instability (upper) and firehose mode (bottom). The black dashed line is the line $T_{\perp}/T_{||}$=1. The two green dashed lines are the line $T_{\perp}/T_{||}$=0.9 and $T_{\perp}/T_{||}$=1.1.

means that the plasma over ion scales is more stable against temperature anisotropy instabilities in the near-Earth plasma sheet than in the midtail region. To further test the physical consequences of temperature anisotropy-driven instabilities, we investigate the occurrence of ion-scale magnetic fluctuations in ($\beta_{||}$, $T_{\perp}/T_{||}$) space.

3.3. The Enhancement of the Magnetic Fluctuation

[16] The spin period of THEMIS spacecraft is 3 s, and we will use the 3 s average magnetic field data as the mean field B_0. With respect to this mean field, we calculate the rms fluctuation field δB of the 4 Hz data, where δB is rotated into a mean field aligned coordinate system. Each fluctuation field measurement δB is rotated into a coordinate system such that we have both the compressive component $\delta B_{||}$ and the shear component $\delta B_{\perp}$. We then define the magnetic compressibility as $(\delta B_{||}/\delta B)^2$ [*Bale et al.*, 2009]. We calculated the average measured amplitude of $\delta B/B_0$ and $(\delta B_{||}/\delta B)^2$ in every bin.

[17] Figure 9 shows the average measured amplitude of the magnetic fluctuation $\delta B/B_0$ in ($\beta_{||}$, $T_{\perp}/T_{||}$) space for all cases.

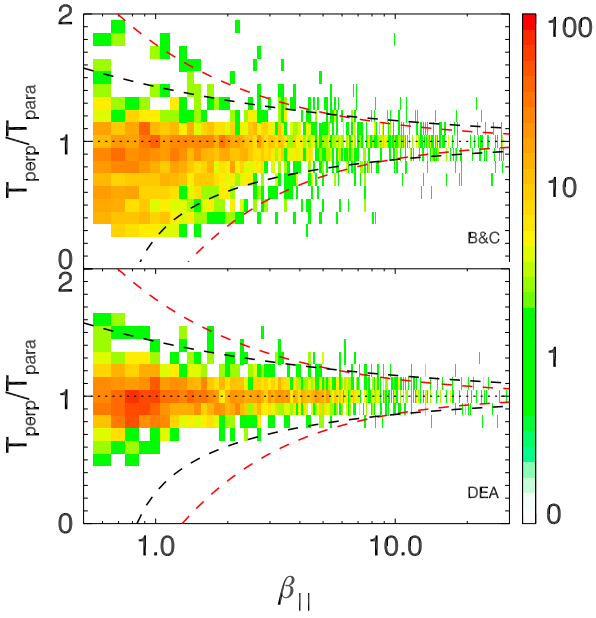

Figure 6. The top panel gives the statistic distribution associated with the BBF of all events in the space ($\beta_{||}$, $T_{\perp}/T_{||}$) observed by THB and THC, and the bottom gives the statistic distribution of the other three spacecraft. The four curves are the thresholds of four instabilities which are same with Figure 5.

Figure 10 shows the magnetic compressibility for the same cases as Figure 9. It is clear in the figures that ion-scale magnetic fluctuations follow the instability threshold curves. In the region $T_{\perp}/T_{||}$>1, it is noticeable that the enhanced magnetic compressibility is along the mirror mode curve,

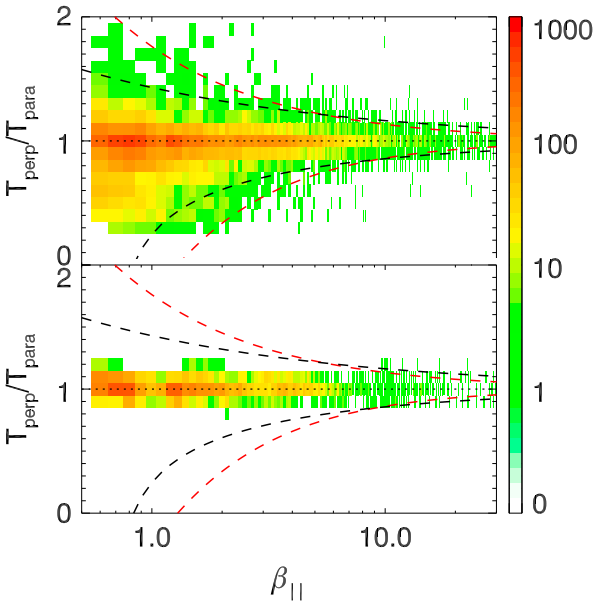

Figure 7. The top panel shows the statistic distribution associated with the BBFs of all events in the space ($\beta_{||}$, $T_{\perp}/T_{||}$), and the bottom panel is the statistic distribution associated with the quiet plasma sheet of all events in the space ($\beta_{||}$, $T_{\perp}/T_{||}$).

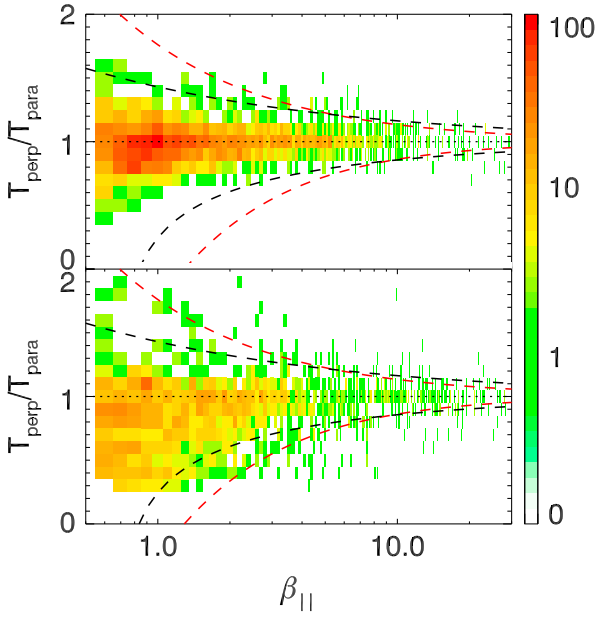

Figure 8. The top panel is the statistic distribution associated with the BBF in the space ($\beta_{||}$, $T_\perp/T_{||}$) observed at $|X\_GSM| < 14R_E$, and the bottom panel is the statistic distribution associated with the BBF in the space ($\beta_{||}$, $T_\perp/T_{||}$) observed at $|X\_GSM| \geq 14R_E$.

whereas the enhanced $\delta B/B_0$ mainly follows the proton cyclotron mode curve. In the region $T_\perp/T_{||}<1$, there seems to be less differentiation, and most of the enhanced magnetic activity seems to be along the two firehose instabilities curves. In the MHD-CGL case, the firehose modes can be unstable when $\beta_{||} - \beta_\perp > 2$ [*Gary et al.*, 1998; *Wang and Hau*, 2003], in which case the parallel firehose instability is noncompressional. Expanding on the MHD-CGL work, either by taking into account cyclotron kinetic effects [*Hellinger and Matsumoto*, 2000] or by modifying the MHD-CGL model with anisotropic heat flux equations [*Dzhalilov et al.*, 2011], will lead to the appearance of the oblique firehose instability, which adheres to the same instability criteria as the original parallel firehose instability, but has its major growth rate under oblique propagation with respect to the magnetic field. One-dimensional (1-D) hybrid simulations show that the oblique firehose instability has density compressibility but no magnetic compressibility [*Hellinger and Matsumoto*, 2000]. Then again, *Dzhalilov et al.* [2011] describe this new Alfvénic mode specifically as a compressible oblique firehose mode resulting from the resonant interaction of two thermal modes and a fast mirror mode. Our results in Figure 10 show that there is some magnetic compressibility (when $T_\perp<T_{||}$) along the red oblique firehose mode curve.

[18] For the cases observed in midtail ($|X\_GSM| \geq 14R_E$), the enhancements of $\delta B/\delta B_0$ mainly follow the proton cyclotron ($T_\perp>T_{||}$) and parallel firehose ($T_\perp<T_{||}$) thresholds, whereas the enhanced magnetic compressibility is mainly along the mirror threshold ($T_\perp>T_{||}$). The results are similar to what Figures 9 and 10 have shown. But for the cases observed in the near-Earth tail ($|X\_GSM| < 14R_E$), the results

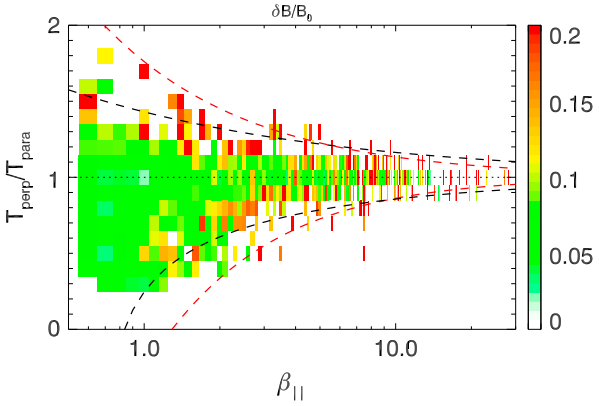

Figure 9. The average measured amplitude of the magnetic fluctuation $\delta B/B_0$ in the space ($\beta_{||}$, $T_\perp/T_{||}$) for all cases.

are different. Figure 11 shows the average measured amplitude of the magnetic fluctuation $\delta B/B_0$ in ($\beta_{||}$, $T_\perp/T_{||}$) space for the cases in the near-Earth region ($|X\_GSM| < 14\ R_E$). Figure 12 shows the magnetic compressibility for the same cases as Figure 11. In Figures 11 and 12, most of the enhanced magnetic activity seems to be only along the mirror mode and proton cyclotron mode curve.

4. Summary and Discussions

[19] We have presented multipoint observations of BBFs by the THEMIS spacecraft, where we concentrated on the development of the proton temperature anisotropy $T_\perp/T_{||}$ along the Earth's magnetotail. We find that as the BBFs move towards the Earth, the proton temperature anisotropy decreases and finally the plasma proton temperature returns to isotropy in the near-Earth tail. All the BBF events in our study are dominated by earthward flows, although some events around 10 R_E down the magnetotail have short intervals of tailward flows. These short tailward flows, however, are almost isotropic and have little effect on our results. To estimate the uncertainty in our temperature ratio, we have used quiet plasma sheet data just before the BBFs, which should have an isotropic temperature [*Runov et al.*, 2010;

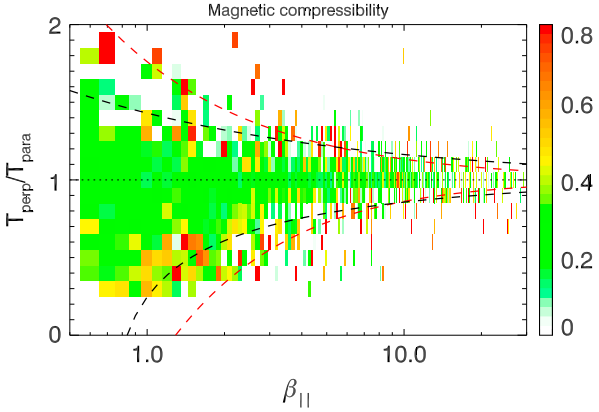

Figure 10. The magnetic compressibility in the space ($\beta_{||}$, $T_\perp/T_{||}$) for all cases.

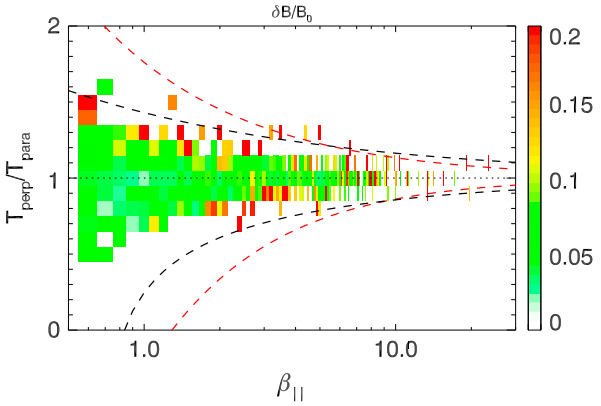

Figure 11. The average measured amplitude of the magnetic fluctuation $\delta B/B_0$ in the space ($\beta_{||}$, $T_\perp/T_{||}$) for the cases observed at $|X\_GSM| < 14R_E$.

Kim et al., 2010]. Our results show that during quiet times, the temperature ratio is $0.9 < T_\perp/T_{||} < 1.1$, so we assume that the error bar on our temperature ratio is ~0.1. *Kaufmann et al*. [2005] pointed out that the proton temperature anisotropy $T_\perp/T_{||}$ increased away from the neutral sheet, reaching 1.1–1.3 at some locations. However, the anisotropy of most of our events is higher than that and the quiet time ratio does not indicate that this is happening. Therefore, we conclude that the distance away from the neutral sheet does not have a significant effect on our conclusions. The effect of Coulomb collisions can also be neglected because the plasma sheet is very hot and tenuous.

[20] In the magnetotail the proton temperature anisotropy can drive instabilities: the mirror mode and proton cyclotron instability for $T_\perp > T_{||}$; the parallel and oblique firehose instabilities for $T_\perp < T_{||}$. The occurrence of the firehose instability seems to be dependent on the location of the spacecraft in the Earth's magnetotail. The separation of the data into regions $|X\_GSM| < 14R_E$ and $|X\_GSM| \geq 14R_E$ shows a significant difference in Figure 6. For the near-Earth region of the tail, the temperature asymmetry does not extend past the firehose mode threshold, whereas further down the tail it does. *Ji and Wolf* [2003] simulated a thin magnetic filament model in the tail using double-adiabatic MHD theory, and found that the firehose instability occurred in the simulation. The strong variations found in the various parameters in the simulation seem to be mainly in the region $|X\_GSM| \geq 14R_E$, which would be consistent with our results. However, *Kim et al*. [2010] also studied the proton temperature anisotropy instabilities with Cluster data. They found the anisotropy often exceeds the mirror instability criterion, but the firehose limit is much less often violated during the BBF interval. Possible reason is that most of their cases reveal a higher temperature in the perpendicular direction than in the parallel direction.

[21] In this paper, we divided the magnetotail into two parts by $|X\_GSM| = 14R_E$. *Nagai et al*. [2005] pointed out the solar wind energy input controls the magnetic reconnection site in the magnetotail. Since one of the sources of BBF associated anisotropy is magnetic reconnection, temporal variations of solar wind energy input may influence the observed location of the strongest anisotropies in the tail. Under different solar wind condition, the parameters used to divide the magnetotail into two parts might be slightly different.

[22] In the magnetotail, the magnetic fluctuation amplitude is mainly enhanced along both the proton cyclotron ($T_\perp > T_{||}$) and parallel firehose ($T_\perp < T_{||}$) thresholds, whereas the enhanced magnetic compressibility is mainly along the mirror mode threshold ($T_\perp > T_{||}$). These compressible fluctuations are evidences for the mirror mode. We also find the evidence of magnetic compressibility near the oblique firehose mode threshold. 1-D hybrid simulation results showed that the oblique firehose mode has no magnetic compressibility [e.g., *Hellinger and Matsumoto*, 2000], but analytical studies showed that there is a new compressional oblique fire hose mode, resulting from a resonant interaction with a mirror mode which could make it magnetically compressional. A detailed study on the magnetic compressibility of this new mode is for future investigations.

[23] The proton distributions departed from the bi-Maxwellian distribution and the nonlinear effects would produce the disagreements between linear predictions used by *Hellinger et al*. [2006] and observations. The linear prediction assumes that the protons have homogeneous bi-Maxwellian distribution. However, the observed proton distribution functions sometimes exhibit departure from the bi-Maxwellian distribution function. The collisionless plasma is susceptible to compressions and expansions which can produce fluctuations of the magnetic field, velocities, and density. These inhomogeneities and the departure from the bi-Maxwellian distribution can influence all four instabilities. If the instabilities develop at a nonlinear level, some properties may exhibit some difference from the linear predictions. For the mirror mode, with the Cluster observations, *Genot et al*. [2009] pointed out that mirror modes and mirror structures can be observed below the linear threshold. And for the oblique firehose instability, *Hellinger and Travnicek* [2008] use 1-D hybrid simulation to confirm that this instability has a self-destructing property and generates stronger wave emissions for larger initial temperature anisotropies. Another possible reason of the disagreements between linear predictions and observations is that there are not enough points near the thresholds of the four instabilities.

[24] Furthermore, more simulation and observation works are needed to study the roles of different instabilities in detail, just like what have already done in the magnetosheath [e.g., *Lacombe and Belmont*, 1995]. This will be our future work.

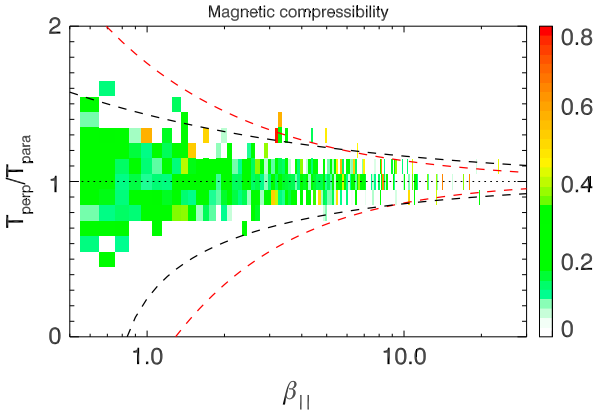

Figure 12. The magnetic compressibility in the space ($\beta_{||}$, $T_\perp/T_{||}$) for the cases observed at $|X\_GSM| < 14R_E$.

[25] **Acknowledgments.** We acknowledge NASA contract NAS502099 for use of data from the THEMIS Mission. This work was supported by 973 Program (2012CB825602), the National Science Foundation of China (NSFC) under grants 41174124 and 41121003, Ocean Public Welfare Scientific Research Project, State Oceanic Administration People's Republic of China (201005017), CAS Key Research Program KZZD-EW-01, and the Fundamental Research Funds for the Central Universities (WK2080000010). The work by Zoltán Vörös was supported by the Austrian Wissenschaftsfonds FWF under grant P24740-N27.

[26] Masaki Fujimoto thanks the reviewers for their assistance in evaluating this paper.

References

Anderson, B. J., S. A. Fuselier, S. P. Gary, and R. E. Denton (1994), Magnetic spectral signatures in the Earth's magnetosheath and plasma depletion layer, *J. Geophys. Res.*, *99*(A4), 5877–5891, doi:10.1029/93JA02827.

Angelopoulos, V. (2008), The THEMIS mission, *Space Sci. Rev.*, *141*, 5–34.

Angelopoulos, V., W. Baumjohann, C. F. Kennel, F. V. Coroniti, M. G. Kivelson, R. Pellat, R. J. Walker, H. Lühr, and G. Paschmann (1992), Bursty Bulk flows in the inner central plasma sheet, *J. Geophys. Res.*, *97*, 4027–4039.

Angelopoulos, V., C. F. Kennel, F. V. Coroniti, R. Pellat, M. G. Kivelson, R. J. Walker, C. T. Russell, W. Baumjohann, W. C. Feldman, and J. T. Gosling (1994), Statistical characteristics of bursty bulk flow events, *J. Geophys. Res.*, *99*, 21257–21280.

Auster, H. U., et al. (2008), The THEMIS fluxgate magnetometer, *Space Sci. Rev.*, *141*, 235–264, doi:10.1007/s11214-008-9365-9.

Bale, S. D., et al. (2009), Magnetic Fluctuation Power Near Proton Temperature Anisotropy Instability Thresholds in the solar wind, *Phys. Rev. Lett.*, *103*, 211101.

Bauer, T. M., et al. (1995), Low-frequency waves in the near-Earth plasma sheet, *J. Geophys. Res.*, *100*, 9605–9617.

Baumjohann, W., G. Paschmann, and H. Lühr (1990), Characteristics of High-Speed Ion Flows in the Plasma Sheet, *J. Geophys. Res.*, *95*, 3801–3809.

Baumjohann, W., G. Paschmann, T. Nagai, and H. Lühr (1991), Superposed epoch analysis of the substorm plasma sheet, *J. Geophys. Res.*, *96*, 11,605–11,608, doi:10.1029/91JA00775.

Baumjohann, W., M. Hesse, S. Kokubun, T. Mukai, T. Nagai, and A. A. Petrukovich (1999), Substorm dipolarization and recovery, *J. Geophys. Res.*, *104*, 24,995–25,000, doi:10.1029/1999JA900282.

Chen, C. X., and R. A. Wolf (1999), Theory of thin-filament motion in Earth's magnetotail and its application to bursty bulk flows, *J. Geophys. Res.*, *104*, 14,613, doi:10.1029/1999JA900005.

Drake, J. F., M. Swisdak, T. D. Phan, P. A. Cassak, M. A. Shay, S. T. Lepri, R. P. Lin, E. Quataert, and T. H. Zurbuchen (2009), Ion heating resulting from pickup in magnetic reconnection exhausts, *J. Geophys. Res.*, *114*, A05111, doi:10.1029/2008JA013701.

Dzhalilov, N. S., V. D. Kuznetsov, and J. Staude (2011), Wave instabilities of a collisionless plasma in fluid approximation, Contrib, *Plasma Phys.*, *51*(7), 621–638, doi:10.1002/ctpp.201000089.

Gary, S. P., S. A. Fuselier, and B. J. Anderson (1993), Ion anisotropy instabilities in the magnetosheath, *J. Geophys. Res.*, *98*, 1481–1488.

Gary, S. P., M. E. McKean, D. Winske, B. J. Anderson, R. E. Denton, and S. A. Fuselier (1994), The proton cyclotron instability and the anisotropy/β inverse correlation, *J. Geophys. Res.*, *99*, 5903–5914.

Gary, S. P., H. Li, S. O'Rourke, and D. Winske (1998), Proton resonant firehose instability: Temperature anisotropy and fluctuating field constraints, *J. Geophys. Res.*, *103*, 14,567–14,574.

Genot, V., et al. (2009), Mirror structures above and below the linear instability threshold: Cluster observations, fluid model and hybrid simulations, *Ann. Geophys.*, *27*, 601–615.

Goertz, C. K., and W. Baumjohann (1991), On the thermodynamics of the plasma sheet, *J. Geophys. Res.*, *96*, 20,991–20,998.

Hasegawa, A. (1969), Drift Mirror instability in the magnetosphere, *Phys. Fluids*, *12*, 2642.

Hellinger, P., and H. Matsumoto (2000), New kinetic instability: Oblique Alfven fire hose, *J. Geophys. Res.*, *105*, 10,519–10,526.

Hellinger, P., and P. Travnicek (2008), Oblique proton fire hose instability in the expanding solar wind: Hybrid simulations, *J. Geophys. Res.*, *113*, A10109, doi:10.1029/2008JA013416.

Hellinger, P., P. Travnicek, J. C. Kasper, and A. J. Lazarus (2006), Solar wind proton temperature anisotropy: Linear theory and WIND/SWE observations, *Geophys. Res. Lett.*, *33*, L09101, doi:10.1029/2006GL025925.

Ji, S., and R. A. Wolf (2003), Double-adiabatic MHD theory for motion of a thin magnetic filament and possible implications for bursty bulk flows, *J. Geophys. Res.*, *108*(A5), 1191, doi:10.1029/2002JA009655.

Kasper, J. C., A. J. Lazarus, and S. P. Gary (2002), Wind/SWE observations of firehose constraint on solar wind proton temperature anisotropy, *Geophys. Res. Lett.*, *29*(17), 1839, doi:10.1029/2002GL015128.

Kaufmann, R. L., W. R. Paterson, and L. A. Frank (2005), Relationships between the ion flow speed, magnetic flux transport rate, and other plasma sheet parameters, *J. Geophys. Res.*, *110*, A09216, doi:10.1029/2005JA011068.

Kim, H.-S., D.-Y. Lee, S.-I. Ohtani, E.-S. Lee, and B.-H. Ahn (2010), Some statistical properties of flow bursts in the magnetotail, *J. Geophys. Res.*, *115*, A12229, doi:10.1029/2009JA015173.

Lacombe, C., and G. Belmont (1995), Waves in the Earth's magnetosheath: Observations and interpretations, *Adv. Space Res.*, *15*, 329–340.

Liu, Y., J. D. Richardson, J. W. Belcher, J. C. Kasper, and H. A. Elliott (2006), Thermodynamic structure of collisiondominated expanding plasma: Heating of interplanetary coronal mass ejections, *J. Geophys. Res.*, *111*, A01102, doi:10.1029/2005JA011329.

Lu, Q. M., and S. Wang (2005), Formation of He2+ shell-like distributions downstream of the Earth's bow shock, *Geophys. Res. Lett.*, *32*, L03111, doi:10.1029/2004GL021508.

Lu, Q. M., F. Guo, and S. Wang (2006), Magnetic spectral signatures in the terrestrial plasma depletion layer: Hybrid simulations, *J. Geophys. Res.*, *111*, A04207, doi:10.1029/2005JA011405.

McFadden, J. P., C. W. Carlson, D. Larson, V. Angelopoulos, M. Ludlam, R. Abiad, B. Elliot, P. Turin, and M. Marckwordt (2008), The THEMIS ESA plasma instrument and in-flight calibration, *Space Sci. Rev.*, *141*, 277–302.

Nagai, T., M. Fujimoto, R. Nakamura, W. Baumjohann, A. Ieda, I. Shinohara, S. Machida, Y. Saito, and T. Mukai (2005), Solar wind control of the radial distance of the magnetic reconnection site in the magnetotail, *J. Geophys. Res.*, *110*, A09208, doi:10.1029/2005JA011207.

Nakamura, R., et al. (2004), Spatial scale of high-speed flows in the plasma sheet observed by Cluster, *Geophys. Res. Lett.*, *31*, L09804, doi:10.1029/2004GL019558.

Quest, K. B., and V. D. Shapiro (1996), Evolution of the fire-hose instability: Linear theory and wave-wave coupling, *J. Geophys. Res.*, *101*, 24,457–24,469.

Runov, A., et al. (2010), Dipolarzation fronts in the magnetotail plasma sheet, *Planet. Space Sci.* , doi:10.1016/j.pss.2010.06.006.

Volwerk, M., et al. (2004), Compressional waves in the Earth's neutral sheet, *Ann. Geophys.*, *22*, 303–315.

Vörös, Z. (2011), Magnetic reconnection associated fluctuations in the deep magnetotail: ARTEMIS results, *Nonlinear Process. Geophys.*, *18*, 861–869.

Vörös, Z., W. Baumjohann, R. Nakamura, A. Runov, M. Volwerk, and T. L. Zhang (2004), Wavelet analysis of magnetic turbulence in the Earth's plasma sheet, *Phys. Plasmas*, *11*, 1333–1338.

Wang, B. J., and L. N. Hau (2003), MHD aspects of fire-hose type instabilities, *J. Geophys. Res.*, *108*(A12), 1463, doi:10.1029/2003JA009986